Solution Processable Barrier Films Using A Filled Polymer to Encapsulate Flexible Printed Electronics

Zehua Chen*†, Ulrich Gengenbach†, Shant Gananian‡, Daniel Moser† , Klaus-Martin Reichert†, Liyu Huang†, and Liane Koker†

†Institute for Automation and Applied Informatics (IAI), Karlsruhe Institute of Technology (KIT), Eggenstein-Leopoldshafen, Germany

‡Project, Process, and Quality Management (PPQ), Karlsruhe Institute of Technology (KIT), Eggenstein-Leopoldshafen, Germany

*zehua.chen@kit.edu

***Abstract*—Flexible printed electronics (FPE) are gaining attention due to their diverse applications, including smart packaging, medical and wearable devices. A key aspect in ensuring the longevity and functionality of FPE devices is their encapsulation, which shields them from adverse environmental factors such as humidity and oxygen. One promising approach to achieve this is solution-processed encapsulation, where fillers are added into a polymer matrix to form barrier films. In this work, glass flakes, graphene oxide, montmorillonite, and silica are investigated as possible fillers in poly(vinyl alcohol) (PVA). The barrier films are fabricated by doctor blading. To select the most effective filler type, a water vapor transmission rate (WVTR) test method based on an adapted desiccant method from the ASTM E96/E96M - 22 standard is developed. The optimal filler concentration in PVA is also determined. The fabricated barrier films are optically inspected. Moreover, the barrier effect of selected PVA/filler films is validated by resistance measurements of inkjet printed silver tracks subjected to damp heat and room storage conditions.**

***Index Terms*—printed electronics, solution-processed encapsulation, barrier films, inorganic fillers, doctor blading, WVTR**

I. Introduction

Additive manufacturing is nowadays established as standard process to produce mechanical parts using the so-called 3D-printing [1], [2]. Another emerging technology is functional printing of electronic devices, sensors, and entire printed circuits [3]–[6].

The properties of novel functional inks, that are frequently based on nanomaterials, enable a variety of new functionalities and applications. Conductive tracks, resistors, insulators, capacitors, coils, and antennas can be manufactured by functional printing as well as various different types of sensors [7]–[10] and a wide range of active devices such as transistors, diodes, and display elements. Further printable devices are solar cells, batteries, and piezoelectric elements [11]–[15].

The devices are printed onto many different types of substrates like flexible foils, textiles, paper and degradable materials or even 3D-surfaces [8], [16], [17]. Here, the focus lies upon flexible printed electronics (FPE) printed on polymer foils. Typically applied printing technologies are screen printing, and digital printing processes like inkjet-printing and aerosol-printing [11], [17]–[19]. Fields of application of the printed electronic devices and systems include medical devices, wearables, smart packages, and textiles [11], [19], [20].

Still, there are several challenges. One of them is the sensitivity of the printed electronics to environmental influences, especially oxygen and humidity [21]–[23]. One reason for that is the large area of printed electronics in comparison to silicon devices, that is even increased by the use of overprinting to avoid boundary effects for multilayer devices [24], [25]. Consequently, depending on the applied printed materials, the thin printed layers exposed to ambient conditions are at risk of degradation. Another observed effect is the influence of absorbed water on the electrical properties of the printed devices, especially when using polymer-based inks [26]. Thus, depending on the application, printed electronics should be well encapsulated while preserving the flexibility of the FPE devices and circuits.

Encapsulation methods for FPE are classified into barrier film lamination, vacuum-deposited thin film encapsulation, and solution-processed encapsulation [27]. When applying the barrier film lamination method, a barrier film is attached to the substrate or to the components by adhesion, thermal bonding, or laser welding. One drawback of this method lies in the fact that a conformal encapsulation on non-planar surfaces is not possible. With vacuum-deposited thin film encapsulation, on the other hand, a thin layer consisting e.g. of Parylene C, SiO_2, or Al_2O_3 is applied by chemical vapor deposition (CVD), or by atomic layer deposition (ALD) respectively. Water vapor transmission rates (WVTR) as low as $10^{-5}\,\mathrm{g\,m^{-2}\,d^{-1}}$ [28] can be achieved by such barrier films. Still, these processes require expensive and complex vacuum equipment such as an ALD reactor.

The approach used in this work is solution-processed encapsulation. Due to its low cost and ease of processing, it is a promising method [27]. Polymers are used for direct formation of barrier films on the devices' surface. The flexible polymer layers are advantageous for FPE. The resulting WVTRs are however orders of magnitude higher than the above mentioned

This paper is an expanded version of https://ieeexplore.ieee.org/document/10603898. This work is funded by the program Material Systems Engineering (MSE) of the Helmholtz Association.

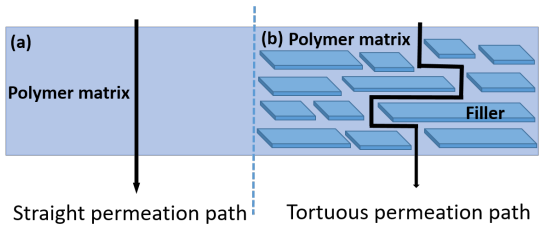

Fig. 1. (a) Straight permeation path through a polymer matrix, (b) tortuous path resulting from lamellar fillers in the polymer matrix

methods but still adequate for various applications [29], [30]. One approach to improve such a polymer based encapsulation is the combination with fillers of less permeable inorganic materials such as glass flakes. The barrier properties are then defined by the material properties and the length of the resulting tortuous path. The latter increases the permeate's effective permeation path through the polymer matrix as shown in Fig. 1 [31]. Thus, by the use of inorganic fillers, the WVTR of the polymer layer is substantially increased without significantly reducing its flexibility.

Various technologies of printing or coating can be applied to form barrier films, e.g., inkjet printing, screen printing, dispensing, doctor blading and spin coating. When using application processes such as dispensing or ink-jet printing, solution-processed encapsulation yields the potential for conformal coating. Two commonly used polymer matrices described in the literature are poly(vinyl alcohol) (PVA) [32]–[37] and poly(vinyl butyral) (PVB) [30], [38]. Both are non-toxic and easy to process. Furthermore, PVA itself already yields high barrier properties against O_2.

To increase the tortuosity of the permeation path, different fillers are applied, such as montmorillonite (MMT) [37], [39], [40], glass flakes [30], [34], [38], graphene oxide (GO) [41], zinc oxide [35]. Chandio et al. utilized sodium montmorillonite ($MMT\text{-}Na^+$) clay as filler material in PVA and reached a WVTR of $2.8\,\mathrm{g\,m^{-2}\,d^{-1}}$ for the $PVA/MMT\text{-}Na^+$ ($10\,\mathrm{wt\%}$) film under test conditions of $85\,\%\mathrm{RH}$ and $40\,^\circ\mathrm{C}$ [37]. Channa et al. used glass flakes (GF) as fillers in PVA. The WVTR of the barrier films was within the range of $6.2\,\mathrm{g\,m^{-2}\,d^{-1}}$ to $1.2\,\mathrm{g\,m^{-2}\,d^{-1}}$ with GF concentrations of 5–25 vol% [34]. A comparison of the applied fillers is, however, not provided. Yu et al. utilized synthesized non-toxic layered double hydroxide (LDH) nanosheets as fillers in cross-linked PVA. The reported WVTR of the PVA/LDH coated PET film is $0.04\,\mathrm{g\,m^{-2}\,d^{-1}}$ [42].

Hereafter, we introduce systematic investigations based upon PVA as the polymer matrix and four commercially available fillers (GF, GO, MMT, and silica) added to PVA solutions at various concentrations. An adapted WVTR test method based on the desiccant method as specified in the ASTM E96/E96M-22 standard was developed to assess moisture barrier performance of the prepared barrier films. To select the most promising filler materials and their respective optimal concentration, WVTR tests are conducted. Moreover, the chosen PVA/filler solution is directly applied as encapsulation material. The barrier effect of the resulting films is validated by measuring resistance changes of inkjet printed silver tracks following damp heat testing and room storage [43]. The microstructure of PVA/filler barrier film is optically inspected.

II. Experimental Section

A. Materials and Methods

PVA (molecular weight: 146000 - 186000, Sigma-Aldrich) was appplied as polymer matrix. Organically modified MMT (Cloisite 20A, BYK ltd), glass flakes (LUXAN F001, Eckart GmbH), silica (Zandosil G220, Heraeus Quarzglas GmbH & Co), and graphene oxide (Sigma Aldrich) were used as fillers. The carrier substrates for selfstanding barrier films preparation were Melinex ST506 (Dupont) polyethylene terephthalate (PET) films. NB-TP-3GU100 PET films (Mitsubishi) were chosen as substrates for inkjet printed silver (Ag) tracks (ink: Silverjet DGP 40LT-15C, Sigma Aldrich).

B. Fabrication of self-standing barrier films

The fabrication process of the self-standing barrier films is shown in Fig. 2. In step 1a, a $5\,\mathrm{wt\%}$ PVA solution utilized as the polymer matrix was prepared by adding $10\,\mathrm{g}$ PVA powder into $190\,\mathrm{g}$ distilled water (DIW). The mixture was heated on a heated magnetic stirrer at $80\,^\circ\mathrm{C}$ for two hours. In step 1b, the filler fraction was prepared by adding the respective

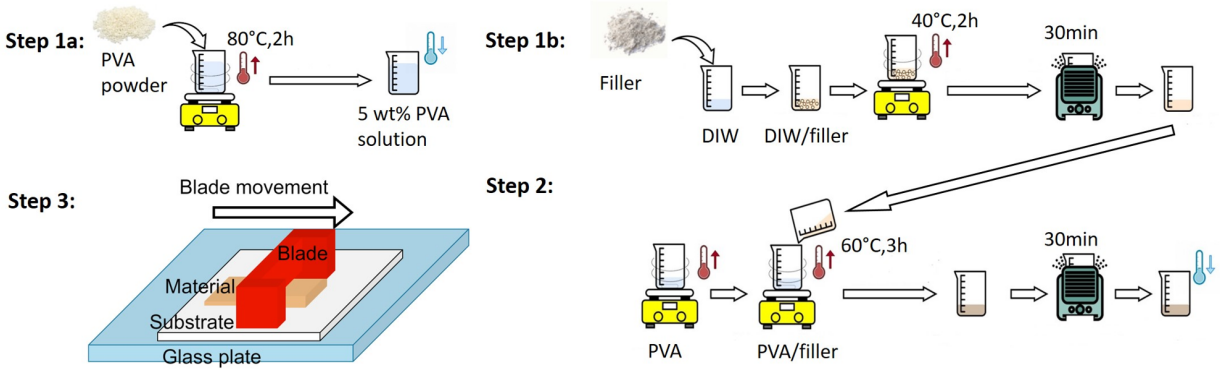

Fig. 2. Fabrication of PVA/filler films. Step 1a: preparation of $5\,\mathrm{wt\%}$ PVA solution applied as polymer matrix; Step 1b: preparation of homogenized DIW/filler suspension; Step 2: preparation of homogenized PVA/filler suspension. Step 3: fabrication of a PVA/filler barrier film on a PET substrate by doctor blading.

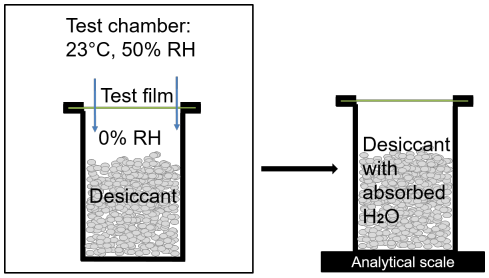

Fig. 3. Schematic illustration of the desiccant method for measuring WVTRs of the test films.

amount of the selected filler material into DIW and stirring with a magnetic stirrer at an elevated temperature of $40\,^{\circ}\mathrm{C}$ for two hours. After an additional $30\,\mathrm{min}$ of ultrasonication, the homogeneous DIW/filler suspension was added to the base PVA solution and stirred at $60\,^{\circ}\mathrm{C}$ for three hours. The resulting PVA/filler suspension was finally ultrasonicated for another $30\,\mathrm{min}$ and cooled down to room temperature (RT) (step 2). These PVA/filler suspensions were doctor bladed on PET carrier substrates with an automatic film applicator (ZAA 2300, ZUA 2000, Proceq); the gap between the blade and the substrate set to $500\,\mu\mathrm{m}$ (step 3). The final dried PVA/GF film measures approximately $11\,\mu\mathrm{m}$. With a hole punch, circular samples (diameter: $12\,\mathrm{mm}$) matching the size of the screw cap used for subsequent WVTR tests were cut from the membranes. Then, the barrier film samples were carefully peeled off the PET carrier substrates.

C. Adapted water vapor transmission rate measurement setup

The desiccant method, as specified by the ASTM-E96 standard [44], provides the basis to assess the moisture barrier properties of PVA/filler films (Fig. 3). This method uses metal test dishes (Fig. 4 (a)) filled with a desiccant sealed with a lid of the material to be tested for permeation. The water permeating through the lid and absorbed by the desiccant is measured by periodic weighing of the test dish. Hence, it is a simple testing apparatus that does not require sophisticated equipment. On the other hand, it yields only limited accuracy (up to two-digit coefficients of variation (CV)) as illustrated by the measurement examples in the standard.

The desiccant method was selected and adapted to our sample dimensions. As the established test dishes are too large to fit our barrier films (Fig. 4 (a)), we selected glass vials (diameter: $14.7\,\mathrm{mm}$) with screw caps with a central hole (diameter: $8.7\,\mathrm{mm}$) (Fig. 4 (b)). These glass vials were partially filled with a desiccant up to approximately 2/3 of their volume. To accommodate the mechanical sensitivity of the thin barrier films, we selected sealing with gaskets from the different sealing solutions suggested in the standard. Thus, the barrier film samples were put between two gaskets and clamped onto the glass vials by the screw cap. To assess moisture absorption by and permeation through the gaskets and caps, three control vials were prepared with $200\,\mu\mathrm{m}$ thick stainless steel sheet metal plates clamped between the gaskets. These control vials were subjected to the same test conditions as the PVA/filler samples, to comprehensively assess the impact of potential variables on the measured results. The weight changes of the vials were measured with an analytical scale Sartorius ED224s with a resolution of $0.1\,\mathrm{mg}$. The weight changes of the control vials were subtracted from the measurements of the film samples. This adapted desiccant method enables the measurement of WVTRs for different barrier films with small sample diameters under identical test conditions in the same test run. The WVTR tests for filler selection were conducted at test conditions of $23\,^{\circ}\mathrm{C}$ and $50\,\%\mathrm{RH}$. A specific type of PVA/filler barrier film exhibiting the lowest water vapor permeability was then chosen. Further tests were then conducted under varying test conditions ($23\,^{\circ}\mathrm{C}$ $50\,\%\mathrm{RH}$; $38\,^{\circ}\mathrm{C}$ $50\,\%\mathrm{RH}$; $38\,^{\circ}\mathrm{C}$ $65\,\%\mathrm{RH}$) to determine the most suitable filler ratio in the suspension.

D. Test structures and test conditions

Fig. 5 shows the conductor structure used for the coating test printed with Ag nanoparticle ink on an Autodrop Gantry inkjet printer (MD-K-140 print head). The printing parameters were set to $170\,\mathrm{V}$ voltage, $45\,\mu\mathrm{s}$ pulse width, $7\,\mathrm{mbar}$ vacuum and $50\,\mu\mathrm{m}$ drop distance. This structure was printed in two passes on PET substrates under ambient conditions and subsequently left to dry at room temperature for seven days. The test structure consists of a central 45 mm conductor with long contact pads on both ends for four-point resistance measurement. The Ag nanoparticle ink used exhibits after printing a substantial sintering effect at low temperatures in a humid environment (cf. [45]). Consequently, the unprotected test structures will show a decrease of resistance once exposed to a humid atmosphere. A protective layer on the central conductor will inhibit the sintering effect of the humid atmosphere and the resulting decrease of resistance. Therefore,

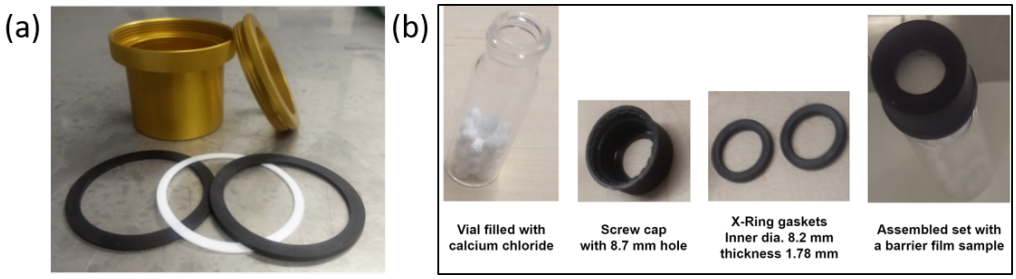

Fig. 4. Development of the adapted desiccant method. (a) The EZ-Cup Vapometer (Thwing-Albert, USA) for measuring WVTR. (b) The adapted desiccant method using small glass vials.

resistance measurement of coated test structures is a method to further quantify the effectiveness of encapsulation. The PVA/filler mixtures were coated onto the central conductor part of the test structures by doctor blading with a gap of $500\,\mu\mathrm{m}$ between blade and substrate and left to dry at RT for one hour. The coated and uncoated test structures were subjected

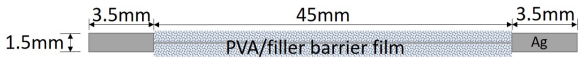

Fig. 5. Schematic illustration of a test structure (inkjet printed Ag track) coated with a PVA/filler barrier film [43].

to a damp heat test in the climate chamber for four days ($40\,^{\circ}\mathrm{C}$, $85\,\%\mathrm{RH}$) and subsequently characterized with four-point resistance measurements (B&K Precision LCR-Meter 981, Formfactor EPS150 probestation with $150\,\mu\mathrm{m}$ probe tips).

E. Optical inspection and analysis of barrier films

The barrier films coated onto the test structures were imaged after damp heat testing with a digital optical microscope (Keyence VHX 7000) with the objective VHX-E100 (DIC OP-88324, polarizer OP-88323 installed) and incident light. The acquired images were processed and analyzed in ImageJ (Version 1.54g). The microscope image was read into ImageJ and its contrast was enhanced with the ImageJ function "Enhance Contrast" with the option "histogram equalization" checked. The resulting image was split into three images, one for each colour channel, with the ImageJ "Colour-Split Channels" function. As the original image had a greenish hue, the green channel showed the best contrast. Hence, the green image was used for further processing with the ImageJ "Adjust threshold" function. The threshold was adjusted to separate the GFs from the background. For most images, a threshold value of about 70% yielded a suitable separation. The separated image served as a basis to calculate the surface area covered by GFs by means of the ImageJ function" Analyse Particles" with its parameters set to "Size (500 µm² -Infinity)" and "include holes". Setting "Size" to start particle counting at 500 µm² allows to exclude image noise from the background of the not GF covered areas and the porosity of the printed Ag tracks. The parameter "include holes" allows to include hole artifacts in GFs resulting from thresholding into the surface area calculation. The visual comparison shows that these parameter settings classify GF covered and non-covered i.e. PVA-only background areas pretty well.

To get further insight into the barrier film inner structure, cross-sections of the film were prepared by ultramicrotome (UM) trimming and inspected under the optical microscope. An UM is a precision instrument to prepare thin sections of embedded samples or precisely cut block faces by means of glass or diamond knives (cf. [46]). The membrane sample is manually cut to size with a razor blade to obtain a smaller rectangular sample for subsequent embedding. The resulting sample is then put into a mold to be embedded in an epoxy resin (Spurr, Sigma-Aldrich, USA) with an optimized recipe to achieve a firm hardness. To properly define the position of the sample in mold and in the resulting epoxy resin block after polymerization, an in-house developed holding structure, 3D printed with polylactic acid (PLA) was used [47]. The membrane sample was placed into the opening of this printed structure and thus stays in place during embedding with the resin. The mold was then subjected to an oven curing process at $70\,^{\circ}\mathrm{C}$ for approximately 16 hours, to achieve full polymerization of the embedding material. Once cooled to room temperature, the resulting sample block was clamped into an ultramicrotome sample holder and manually pre-trimmed with a razor blade to expose the region of the embedded membrane sample to the surface. To facilitate additional precise trimming of the sample block face, an ultramicrotome (Leica EM UC7, Leica Microsystem, Germany) with diamond trimming knife (Trim 90, DiATOME Ltd., Switzerland) was applied. The sectioning speed was set to 6 mm/s, and the sectioning feed was $500\,\mathrm{nm}$. Ultimately, a sample block face of rectangular shape in a size of $899.7\,\mu\mathrm{m} \times 353.5\,\mu\mathrm{m}$ was trimmed. The embedded membrane structure was exposed to the surface in the middle of the block face for subsequent imaging with a digital optical microscope (Keyence VHX 7000).

III. RESULTS

The WVTRs of the fabricated barrier films were characterized with the adapted desiccant method, both, for the selection of the filler material and for the assessment of the barrier properties of the selected materials at different concentrations. The results show CV levels of our measurements (up to 40%) that match the values outlined in the standard. This indicates the validity of the adapted desiccant method.

A. Filler selection

Four fillers are added to a $5\,\mathrm{wt}\%$ PVA solution at different ratios to prepare barrier films. The WVTR of each film is measured using the adapted desiccant method. As shown in Fig. 6, adding $5\,\mathrm{wt}\%$ GF yields better moisture barrier properties compared to adding $20\,\mathrm{wt}\%$ GF into the PVA solution. Kapila et al. report a significant elongation at break (EAB)

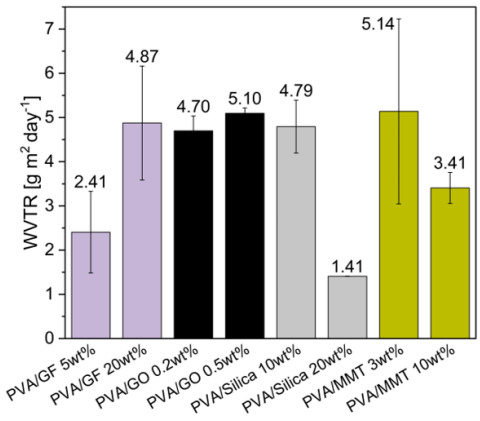

Fig. 6. WVTRs of various PVA/filler films for the filler selection. Error bars represent standard deviations.

of the PVA/GO films as the concentration of GO increases from $0.1\,\%$ to $0.3\,\%$ and decreases significantly with further addition of GO from $0.3\,\%$ to $0.7\,\%$ [36]. Thus, PVA/GO

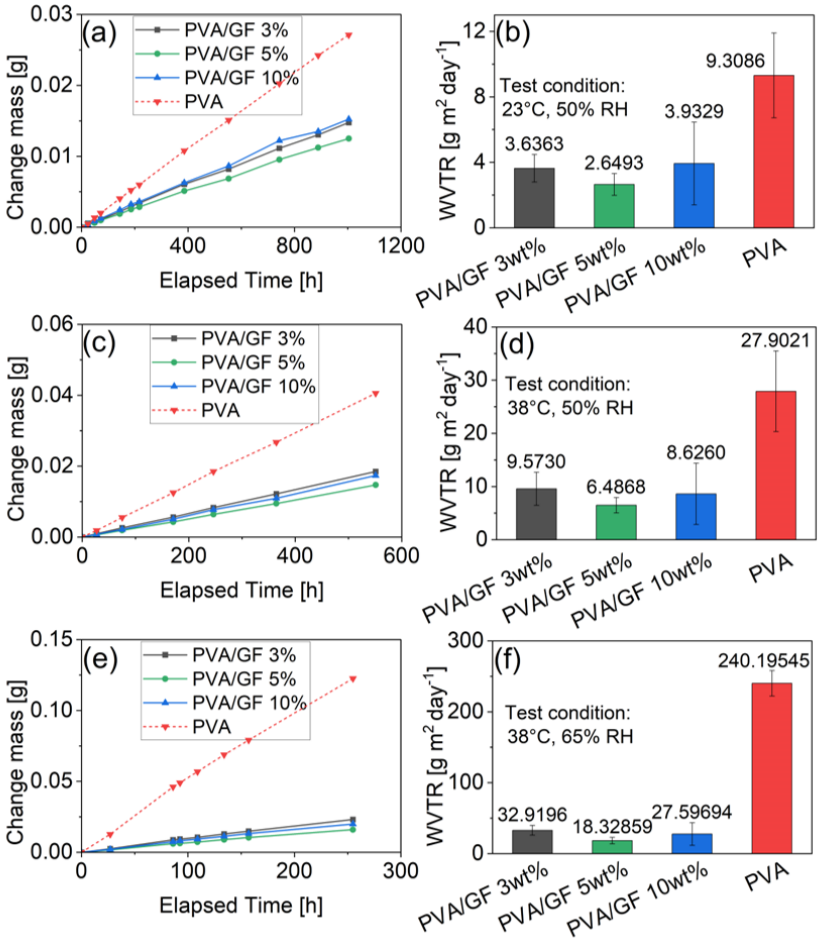

Fig. 7. PVA/GF films with different GF concentrations. (a), (c), (e): weight change of the test dishes with PVA/GF films under three test conditions. (b), (d), (f): Resulting WVTRs of PVA/GF films under three test conditions (error bars represent standard deviations).

films are produced by adding $0.2\,\mathrm{wt\%}$ and $0.5\,\mathrm{wt\%}$ GO in the PVA solution, respectively. The PVA/GO barrier films show a lower barrier performance than the PVA/GF $5\,\mathrm{wt\%}$ films. Moreover, adding GO turns PVA films into black layers, which limits their applicability in applications requiring light transmission. Adding $20\,\mathrm{wt\%}$ silica to the PVA solution yields the best moisture barrier property. However, both by adding $10\,\mathrm{wt\%}$ and $20\,\mathrm{wt\%}$ silica to the PVA solution, the produced PVA/Silica films are relatively brittle compared to the other three types of films, thus not suitable for application on flexible substrates. PVA/MMT barrier films show enhanced moisture barrier performance with increasing MMT content. However, the moisture barrier effect of our films prepared by adding $10\,\mathrm{wt\%}$ MMT is not as good as that of the films with only $5\,\mathrm{wt\%}$ GF added. The MMTs tend to agglomerate more than GFs in the film fabrication process, due to the hydrophilicity of the MMT type used. Hence, the filler aspect ratio ultimately achieved is more favorable for GFs, which is beneficial for increasing the effective permeation path [34]. Therefore, GFs are selected as filler material for further tests.

B. WVTR tests for PVA/GF films

GFs at concentrations of $3\,\mathrm{wt\%}$, $5\,\mathrm{wt\%}$, and $10\,\mathrm{wt\%}$ are added to the PVA solution to fabricate barrier films. The WVTRs of five films of each concentration are measured using the adapted desiccant method under three test conditions: $23\,^{\circ}\mathrm{C}$, $50\,\%\mathrm{RH}$; $38\,^{\circ}\mathrm{C}$, $50\,\%\mathrm{RH}$; and $38\,^{\circ}\mathrm{C}$, $65\,\%\mathrm{RH}$. The weight changes are recorded as shown in Fig. 7 (a), (c) and (e). The linear increase in the mass of the test dishes again indicates the validity of the adapted desiccant method. Compared with the pure PVA films, adding GFs in PVA can significantly improve the moisture barrier property by more than one order of magnitude (Fig. 7 (b), (d), and (f)). However, a higher GF content appears to reduce the homogeneity of the resulting PVA/GF films. It is assumed that adding GFs at concentration of $10\,\mathrm{wt\%}$ in PVA solution results in some GFs remaining partially exposed to the air after drying, rather than being fully embedded within the PVA matrix, thus resulting in the increased WVTR and standard deviation compared to films with $5\,\mathrm{wt\%}$ GFs. Across all test conditions, PVA/GF films containing $5\,\mathrm{wt\%}$ GFs yield the lowest WVTR. Thus, PVA solutions containing $5\,\mathrm{wt\%}$ GFs are applied as the encapsulation material for the test structures.

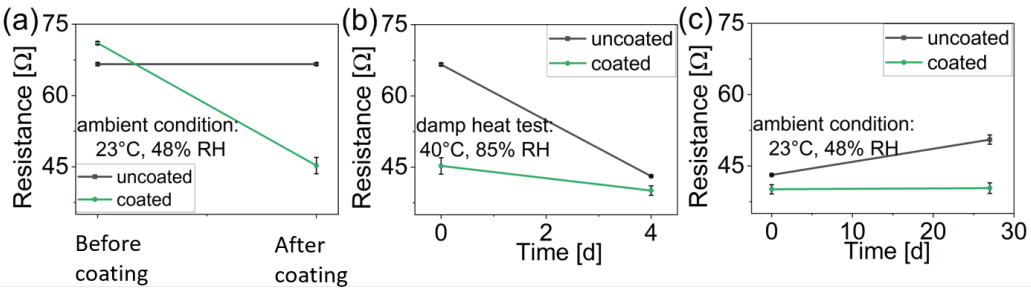

Fig. 8. Resistance of uncoated vs. PVA/GF-coated test structures. (a) before and after coating; (b) after four days of damp heat test; and (c) after 27 days of room storage after damp heat test. Error bars represent standard deviations.

C. PVA/GF encapsulation of test structures

The results of the resistance measurements of coated and uncoated printed test structures (three samples each) are shown in Fig. 8. A group of uncoated test structure samples serves as reference and yields the resistance of $(66.01 \pm 0.26)\,\Omega$. PVA suspension containing $5\,\mathrm{wt}\%$ GF is directly coated on top of inkjet printed Ag tracks under ambient conditions. Before encapsulation, the samples yield a resistance of $(71.02 \pm 0.34)\,\Omega$, after encapsulation, the resistance drops to $(45.27 \pm 1.74)\,\Omega$. This resistance drop can be attributed to the water sintering effect of silver nanoparticle ink reported in [45]. Here, the same silver NP ink and substrate are utilized, therefore, water sintering should also occur and lead to a respective resistance drop. We assume the PVA might interact with the silver nanoparticle capping agent, further promoting the water sintering effect. However, further investigation is required to confirm this assumption.

These two groups of samples are then subjected to damp heat conditions ($40\,^{\circ}\mathrm{C}$ & $85\,\%\mathrm{RH}$) for four days. After the damp heat test, the resistance of uncoated samples drops sharply by $34.7\,\%$ to $(43.11 \pm 0.12)\,\Omega$ due to the damp heat sintering effect reported in literature [45], [48]. The resistance decrease due to this sintering effect occurs to a lesser degree in the coated samples. The resistance of the coated samples drops only by $11.5\,\%$. After the damp heat test, both uncoated and coated samples are stored under ambient conditions. After 27 days of storage, the resistance of uncoated samples increases to $(50.54 \pm 0.97)\,\Omega$ while the resistance change of the coated samples is negligible ($0.58\,\%$), which indicates the barrier effect of the PVA/GF film.

D. Microstructure of the PVA/GF film

Nine top view microscope images, $2\,\mathrm{mm} \times 3\,\mathrm{mm}$ each, were taken from one sample with the coated test structures, three (left edge, middle, right edge) on the middle printed line and three more below and above, respectively (figure 9 (a)). From these nine microscope images figure 9 (b)-(d)) shows three examples. These microscope images indicate that the distribution of the glass flakes in the film varies from multiple glass flakes stacked on top of each other, to regions with a layer of disconnected single glass flakes or no glass flakes at all and thus pure PVA only. To quantify a GF coverage rate, the microscope images were analyzed by means of ImageJ (see section II-E). The analysis yields a coverage rate from $60\,\%$ over the printed track (see e.g. Fig. 9 (f)) to $80\,\%$ over the substrate (see Fig. 9 (g)). The influence of the printed silver tracks' thickness of ca. $1\,\mu\mathrm{m}$ is negligible in comparison to the PVA/GF film thickness during the coating process. Hence, the observed reduced coverage of the PVA/GF coating on top of the printed silver tracks is attributed to reduced wetting on the silver surface. The average coverage rate is $72\,\%$ with a variance of $5.9\,\%$ across all images (see e.g. Fig. 9 (e) with a coverage rate of $73\,\%$). Neither in lateral (doctor blade width), nor in longitudinal direction, a larger variance is observed. With respect to the absolute GF coverage rates, it should, however, be taken into account that some single GFs parallel aligned to the substrate plane are not properly detected by the ImageJ image processing due to low contrast. Thus, it is likely that these coverage rates are underestimated by a few percent. To get insight into the GF arrangement in the film cross-section, a block face was prepared and imaged as outlined in section II-E. The microscope images of the PVA/GF-film block face exhibit a lamellar arrangement of the glass flakes with only few agglomerations (Fig. 10). Dimensional measurements on the glass flakes yield thicknesses between about $0.9\,\mu\mathrm{m}$ and $2.3\,\mu\mathrm{m}$. The longitudinal dimensions observed match the specification by the supplier ($180\,\mu\mathrm{m}$ to $200\,\mu\mathrm{m}$ (D_{50} percentile of the particle size distribution) [49]. The images confirm a favorable aspect ratio of the glass flakes and a resulting significantly increased tortuosity of the permeation path. Moreover, they show that the GF size and their size distribution have an influence on the formation and porosity of the PVA/GF coating. Thinner GFs would yield a higher number of stacked GFs. A wider distribution range of their longitudinal dimensions could increase the probability that smaller GFs fill the gaps between larger GFs reducing the porosity of the resulting PVA/GF coating and thus, its WVTR.

IV. Conclusion

In this work, GF, GO, MMT, and silica as filler materials are compared in a PVA matrix. An adapted desiccant method for WVTR measurement based on the ASTM E96/E96M-22 standard is developed for WVTR assessments of the PVA/filler barrier films. Among four fillers, GF emerges as the most suitable filler. PVA/GF films containing $5\,\mathrm{wt}\%$ GFs yield the lowest WVTR and are then applied as the encapsulation layer

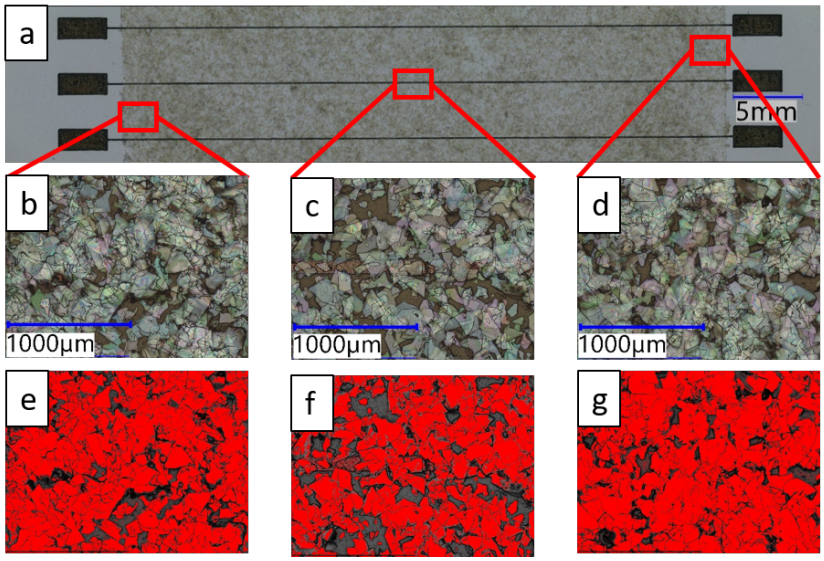

Fig. 9. Optical inspection of PVA/GF-coated printed Ag tracks on a NB-TP-3GU100 PET substrate. (a) Top view of PVA/GF-coated test structures. Microscope images are taken from (b) the area below the printed Ag tracks, (c) the middle of the coated printed Ag tracks, and (d) the area above the printed Ag tracks. (e) - (g): Processed microscope images by ImageJ to quantify GF coverage rates, corresponding to (b) - (d) respectively.

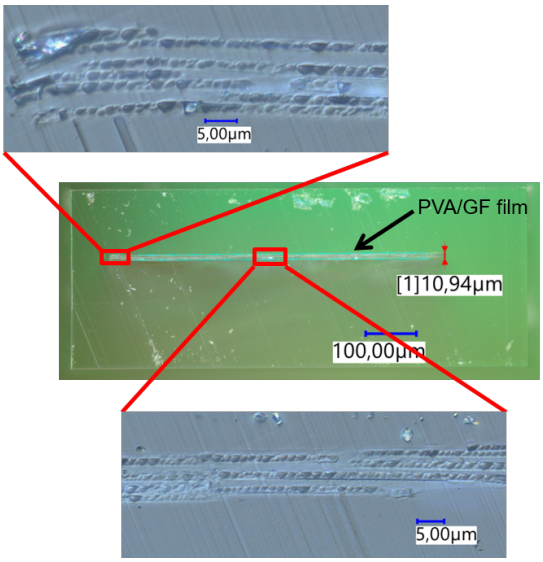

Fig. 10. Microscope image of the PVA/GF barrier film block face exhibits a lamellar arrangement of the glass flakes with only few agglomerations and a resulting tortuous path in the PVA matrix.

directly coated onto the test structures. The moisture barrier effect of this encapsulation layer is validated by measuring resistance changes of inkjet printed Ag tracks after damp heat test and room storage conditions. One sample of the PVA/GF coated test structures is optically inspected and GF coverage rates are quantified by image processing via ImageJ. The average coverage rate is $72\,\%$ with a variance of $5.9\,\%$ among nine top view microscope images. Moreover, the microscope image of a block face of a PVA/GF barrier film confirms the lamellar arrangement of the glass flakes with only few agglomerations and a resulting tortuous path in the PVA matrix. In the next steps, these film properties must be verified on a larger number of samples. Additionally, the mechanical bendability and reliability of the developed barrier films coated onto printed structures must be investigated.

REFERENCES

[1] T. D. Ngo, A. Kashani, G. Imbalzano, K. T. Nguyen, and D. Hui, "Additive manufacturing (3d printing): A review of materials, methods, applications and challenges," *Composites Part B: Engineering*, vol. 143, pp. 172–196, 2018. [Online]. Available: https://www.sciencedirect.com/science/article/pii/S1359836817342944

[2] A. Elkaseer, K. J. Chen, J. C. Janhsen, O. Refle, V. Hagenmeyer, and S. G. Scholz, "Material jetting for advanced applications: A state-of-the-art review, gaps and future directions," *Additive Manufacturing*, vol. 60, p. 103270, 2022. [Online]. Available: https://www.sciencedirect.com/science/article/pii/S2214860422006595

[3] P. Martins, N. Pereira, A. C. Lima, A. Garcia, C. Mendes-Filipe, R. Policia, V. Correia, and S. Lanceros-Mendez, "Advances in printing and electronics: From engagement to commitment," *Advanced Functional Materials*, vol. 33, no. 16, feb 2023.

[4] T. T. Baby *et al.*, "Printing Technologies for Integration of Electronic Devices and Sensors," in *Functional Nanostructures and Sensors for CBRN Defence and Environmental Safety and Security*, ser. NATO Science for Peace and Security Series C: Environmental Security. Springer Netherlands, 2020, pp. 1–34.

[5] U. Gengenbach, M. Ungerer, L. Koker, K.-M. Reichert, P. Stiller, S. Allgeier, B. Köhler, X. Zhu, C. Huang, and V. Hagenmeyer, "Automated fabrication of hybrid printed electronic circuits," *Mechatronics*, vol. 70, p. 102403, oct 2020.

[6] H. Abdolmaleki, P. Kidmose, and S. Agarwala, "Droplet-based techniques for printing of functional inks for flexible physical sensors," *Advanced Materials*, vol. 33, no. 20, p. 2006792, mar 2021.

[7] S. C. Mukhopadhyay *et al.*, "Printed and flexible sensors: a review of products and techniques," in *Printed and Flexible Sensor Technology*, ser. 2053-2563. IOP Publishing, 2021, pp. 1–1 to 1–13.

[8] H. W. Tan, T. Tran, and C. K. Chua, "A review of printed passive electronic components through fully additive manufacturing methods," *Virtual and Physical Prototyping*, vol. 11, no. 4, pp. 271–288, 2016.

[9] N. Divakaran *et al.*, "Comprehensive review on various additive manufacturing techniques and its implementation in electronic devices," *Journal of Manufacturing Systems*, vol. 62, pp. 477–502, 2022.

[10] D. Maddipatla, B. B. Narakathu, and M. Atashbar, "Recent progress in manufacturing techniques of printed and flexible sensors: A review," *Biosensors*, vol. 10, no. 12, 2020. [Online]. Available: https://www.mdpi.com/2079-6374/10/12/199

[11] Organic and Printed Electronics Association (OE-A), "White Paper: OE-A Roadmap for Flexible, Organic and Printed Electronics: 9th Edition," Frankfurt am Main, 2023.

[12] X. Zhang *et al.*, "Fully-additive printed electronics: Transistor model, process variation and fundamental circuit designs," *Organic Electronics*, vol. 26, pp. 371–379, 2015.

[13] K.-J. Baeg, M. Caironi, and Y.-Y. Noh, "Toward printed integrated circuits based on unipolar or ambipolar polymer semiconductors," *Advanced Materials*, vol. 25, no. 31, pp. 4210–4244, jun 2013.

[14] M. Hengge, K. Livanov, N. Zamoshchik, F. Hermerschmidt, and E. J. W. List-Kratochvil, "ITO-free OLEDs utilizing inkjet-printed and low temperature plasma-sintered ag electrodes," *Flexible and Printed Electronics*, vol. 6, no. 1, p. 015009, feb 2021.

[15] E. Bihar, D. Corzo, T. C. Hidalgo, D. Rosas-Villalva, K. N. Salama, S. Inal, and D. Baran, "Fully inkjet-printed, ultrathin and conformable organic photovoltaics as power source based on cross-linked PEDOT:PSS electrodes," *Advanced Materials Technologies*, vol. 5, no. 8, p. 2000226, jun 2020.

[16] C. H. Rao *et al.*, "A Review on Printed Electronics with Digital 3D Printing: Fabrication Techniques, Materials, Challenges and Future Opportunities," *J. Electron. Mater.*, vol. 51, no. 6, pp. 2747–2765, 2022.

[17] J. Wiklund, A. Karakoç, T. Palko, H. Yiğitler, K. Ruttik, R. Jäntti, and J. Paltakari, "A review on printed electronics: Fabrication methods, inks, substrates, applications and environmental impacts," *Journal of Manufacturing and Materials Processing*, vol. 5, no. 3, 2021. [Online]. Available: https://www.mdpi.com/2504-4494/5/3/89

[18] M. Ungerer *et al.*, "A reproducible extrusion printing process with highly viscous nanoparticle inks," *Engineering Research Express*, vol. 6, no. 1, 2024, Art. no. 015042.

[19] I. Verboven and W. Deferme, "Printing of flexible light emitting devices: A review on different technologies and devices, printing technologies and state-of-the-art applications and future prospects," *Progress in Materials Science*, vol. 118, 2021, Art. no. 100760.

[20] Y. Khan, M. Garg, Q. Gui, M. Schadt, A. Gaikwad, D. Han, N. A. D. Yamamoto, P. Hart, R. Welte, W. Wilson, S. Czarnecki, M. Poliks, Z. Jin, K. Ghose, F. Egitto, J. Turner, and A. C. Arias, "Flexible hybrid electronics: Direct interfacing of soft and hard electronics for wearable health monitoring," *Advanced Functional Materials*, vol. 26, no. 47, pp. 8764–8775, oct 2016.

[21] S. Gardonio *et al.*, "Degradation of organic light-emitting diodes under different environment at high drive conditions," *Organic Electronics*, vol. 8, no. 1, pp. 37–43, 2007.

[22] A. Benchirouf *et al.*, "Electrical properties of multi-walled carbon nanotubes/pedot:pss nanocomposites thin films under temperature and humidity effects," *Sensors and Actuators B: Chemical*, vol. 224, pp. 344–350, 2016.

[23] G. Cadilha Marques *et al.*, "Influence of humidity on the performance of composite polymer electrolyte-gated field-effect transistors and circuits," *IEEE Transactions on Electron Devices*, vol. 66, no. 5, pp. 2202–2207, 2019.

[24] M. Mikolajek *et al.*, "Direct inkjet printing of dielectric ceramic/polymer composite thick films," *Advanced Engineering Materials*, vol. 17, no. 9, pp. 1294–1301, 2015.

[25] R. D. Deegan *et al.*, "Capillary flow as the cause of ring stains from dried liquid drops," *Nature*, vol. 389, pp. 827–829, 1997.

[26] M. Ungerer, Z. Chen, T. P. Mach, K.-M. Reichert, U. Gengenbach, M. Lindmüller, J. R. Binder, M. Reischl, and L. Koker, "Automated characterisation of printed electronics under adjustable ambient conditions," in *International Semiconductor Conference – CAS 2024*, [Manuscript accepted for publication], pp. 1–4.

[27] Z. Chen, U. Gengenbach, L. Koker, and M. Mansour, "Approaches for solution-processed encapsulation of printed medical wearable devices," *Current Directions in Biomedical Engineering*, vol. 6, no. 3, pp. 131–134, sep 2020.

[28] P. F. Carcia, R. S. McLean, M. H. Reilly, M. D. Groner, and S. M. George, "Ca test of al2o3 gas diffusion barriers grown by atomic layer deposition on polymers," *Applied Physics Letters*, vol. 89, no. 3, Jul. 2006.

[29] L. Sun, K. Uemura, T. Takahashi, T. Yoshida, and Y. Suzuri, "Interfacial engineering in solution processing of silicon-based hybrid multilayer for high performance thin film encapsulation," *ACS Applied Materials & Interfaces*, vol. 11, no. 46, pp. 43 425–43 432, Oct. 2019.

[30] I. A. Channa, A. Distler, M. Zaiser, C. J. Brabec, and H.-J. Egelhaaf, "Thin film encapsulation of organic solar cells by direct deposition of polysilazanes from solution," *Advanced Energy Materials*, p. 1900598, may 2019.

[31] I. A. Channa, A. Distler, B. Scharfe, S. Feroze, K. Forberich, B. Lipovšek, C. J. Brabec, and H.-J. Egelhaaf, "Solution processed oxygen and moisture barrier based on glass flakes for encapsulation of organic (opto-) electronic devices," *Flexible and Printed Electronics*, vol. 6, no. 2, p. 025006, jun 2021.

[32] E. S. Tsurko, P. Feicht, C. Habel, T. Schilling, M. Daab, S. Rosenfeldt, and J. Breu, "Can high oxygen and water vapor barrier nanocomposite coatings be obtained with a waterborne formulation?" *Journal of Membrane Science*, vol. 540, pp. 212–218, Oct. 2017.

[33] X. Zhang, W. Liu, W. Liu, and X. Qiu, "High performance pva/lignin nanocomposite films with excellent water vapor barrier and uv-shielding properties," *International Journal of Biological Macromolecules*, vol. 142, pp. 551–558, Jan. 2020.

[34] I. A. Channa, J. Ashfaq, S. J. Gilani, A. D. Chandio, S. Yousuf, M. A. Makhdoom, and M. N. b. Jumah, "Sustainable and eco-friendly packaging films based on poly (vinyl alcohol) and glass flakes," *Membranes*, vol. 12, no. 7, p. 701, Jul. 2022.

[35] I. A. Channa, J. Ashfaq, S. J. Gilani, A. A. Shah, A. D. Chandio, and M. N. b. Jumah, "Uv blocking and oxygen barrier coatings based on polyvinyl alcohol and zinc oxide nanoparticles for packaging applications," *Coatings*, vol. 12, no. 7, p. 897, Jun. 2022.

[36] K. Kapila, S. Kirtania, L. M. Devi, A. Saikumar, L. S. Badwaik, and M. A. Rather, "Potential perspectives on the use of poly (vinyl alcohol)/graphene oxide nanocomposite films and its characterization," *Journal of Food Measurement and Characterization*, vol. 18, no. 2, pp. 1012–1025, Nov. 2023.

[37] A. Chandio, I. Channa, M. Rizwan, S. Akram, M. Javed, S. Siyal, M. Saleem, M. Makhdoom, T. Ashfaq, S. Khan, S. Hussain, M. Albaqami, and R. Alotabi, "Polyvinyl alcohol and nano-clay based solution processed packaging coatings," *Coatings*, vol. 11, no. 8, p. 942, Aug. 2021.

[38] I. A. Channa, A. D. Chandio, M. Rizwan, A. A. Shah, J. Bhatti, A. K. Shah, F. Hussain, M. A. Shar, and A. AlHazaa, "Solution processed pvb/mica flake coatings for the encapsulation of organic solar cells," *Materials*, vol. 14, no. 10, p. 2496, May 2021.

[39] J. Gaume, C. Taviot-Gueho, S. Cros, A. Rivaton, S. Thérias, and J.-L. Gardette, "Optimization of pva clay nanocomposite for ultra-barrier multilayer encapsulation of organic solar cells," *Solar Energy Materials and Solar Cells*, vol. 99, pp. 240–249, Apr. 2012.

[40] C. Chen, Y. Chen, J. Xie, Z. Xu, Z. Tang, F. Yang, and K. Fu, "Effects of montmorillonite on the properties of cross-linked poly(vinyl alcohol)/boric acid films," *Progress in Organic Coatings*, vol. 112, pp. 66–74, Nov. 2017.

[41] J. You, B. Oh, Y. S. Yun, and H.-J. Jin, "Improvement in barrier properties using a large lateral size of exfoliated graphene oxide," *Macromolecular Research*, vol. 28, no. 8, pp. 709–713, May 2020.

[42] J. Yu, K. Ruengkajorn, D.-G. Crivoi, C. Chen, J.-C. Buffet, and D. O'Hare, "High gas barrier coating using non-toxic nanosheet dispersions for flexible food packaging film," *Nature Communications*, vol. 10, no. 1, Jun. 2019.

[43] Z. Chen, U. Gengenbach, S. Gananian, D. Moser, K.-M. Reichert, and L. Koker, "Investigation of solution processable moisture barrier films based on a polymer and filler materials," in *2024 IEEE International Conference on Flexible and Printable Sensors and Systems (FLEPS)*. IEEE, Jun. 2024, pp. 1–4.

[44] "Atsm e96 standard test methods for water vapor transmission of materials," http://compass.astm.org/ accessed 3.4.2024, 2024.

[45] Z. Chen, U. Gengenbach, L. Koker, L. Huang, T. P. Mach, K. Reichert, R. Thelen, and M. Ungerer, "Systematic investigation of novel, controlled low-temperature sintering processes for inkjet printed silver nanoparticle ink," *Small*, Dec. 2023.

[46] M. A. Hayat, *Principles and Techniques of Electron Microscopy: Biological Applications*, 4th ed. Cambridge, UK: Cambridge University Press, Apr. 2000.

[47] I. Wacker, R. Curticean, D. Ryklin, B. Weidinger, F. Mayer, L.-Y. Huang, J. Hoffmann, M. Islam, N. von Coelln, T. Schmitt *et al.*, "Deconstructing 3D Structured Materials by Modern Ultramicrotomy for Multimodal Imaging and Volume Analysis across Length Scales," *Advanced Functional Materials*, p. 2302025, 2023.

[48] J. Bourassa, A. Ramm, J. Q. Feng, and M. J. Renn, "Water vapor-assisted sintering of silver nanoparticle inks for printed electronics," *SN Applied Sciences*, vol. 1, no. 6, may 2019.

[49] "Eckart gmbh, data sheet of luxan f001," https://www.eckart.net/en/luxan-f001-038013l90, accessed 22.8.2024.